OPEN ACCESS
Journal of Multidisciplinary Applied Natural Science Vol. 6 No. 3 (2026) https://doi.org/10.47352/jmans.2774-3047.464
Check for updates
Research Article

The Impact of Land Artificialization on Vegetation Cover and Land Surface Temperature (LST) in The Greater Constantine

Kahoul Meriem*, Mazouz Toufik, and Kallab Debih Naouel

Received : February 6, 2026	Revised : May 22, 2026	Accepted : July 6, 2026	Online : July 27, 2026

Abstract

Since the mid-1990s, Greater Constantine has undergone rapid and fragmented urbanization driven by population growth and resettlement policies, causing land artificialization, vegetation loss, and microclimatic changes. This study investigates the relationships between urban growth, vegetation cover, and land surface temperature (LST) from 1995 to 2024 using multi-temporal Landsat imagery processed in Google Earth Engine. The methodology combines supervised land-cover classification using the CART algorithm and the Dynamic World dataset, extraction of vegetation and thermal indices (NDVI and LST.), Normality test was evaluated using the Kolmogorov–Smirnov test with Lilliefors correction, revealing non-normal distributions for all variables ($p \leq 0.001$). Therefore, Spearman's rank correlation was used as the primary measure, while Pearson's correlation was included for comparison. The results show a +68.21% increase in built-up areas and a −30.05% decrease in vegetated surfaces over the study period. Land surface temperature increased from 21.4 °C in 1995 to 32.6 °C in 2024, with a peak in 2015 (35.51 °C), partly attributable to El Niño event of that year. Statistical analysis indicates a weak inverse relationship between NDVI and LST (Spearman R^2 = 0.102–0.215) and a positive relationship between NDBI and LST (Spearman R^2 = 0.269–0.349). confirming that surface artificialization exerts a stronger influence on urban warming than vegetation loss alone. Nevertheless, the moderate explanatory power of both indices indicates that additional factors, including urban morphology, topography, and regional climatic forcing, contribute to spatial temperature variability. A key methodological limitation is the use of two distinct classification approaches (CART for 1995–2005; Dynamic World for 2015–2024), which introduces inter-temporal comparability uncertainty that should be considered when interpreting changes. These findings emphasize the need for nature-based urban planning, including green corridors, tree canopy targets, and permeable surface regulations, to reduce surface warming and strengthen climate resilience in rapidly urbanizing Mediterranean cities.

Keywords: Greater Constantine, land artificialization, LST, NDVI, vegetation cover

1. INTRODUCTION

Like all major cities in Algeria, Constantine is facing significant challenges related to urban expansion, largely driven by migration and a substantial natural population increase since independence up to 1987. During this period, the city's population nearly doubled, resulting in a rapid demographic boom that created a strong housing demand difficult to meet, leading to the proliferation of unplanned residential areas [1][2]. Since the 1990s, Constantine has experienced significant urban sprawl, characterized by a rapid and continuous spatial expansion that extends far beyond its historical boundaries [3]. This process of urban sprawl is strongly linked to the saturation of the city center. Consequently, the 2005 Master Plan for Urban Development and Planning (PDAU) sought to regulate this expansion by directing urban growth toward geotechnically suitable areas, such as the Ain El Bey plateau and other less fertile lands [4].

This uncontrolled urban sprawl contributes to soil saturation, the erosion of plant biodiversity, and the rise of local temperatures, thereby promoting the formation of urban heat islands (UHIs). The excessive artificialization of land surfaces alters the local microclimate and increases environmental risks, including landslides in the steeply sloped areas that characterize the Constantinian landscape [5]. The spatial evolution of Greater Constantine, as revealed through multi-temporal land-use, mapping and the analysis of vegetation and thermal indicators over nearly three decades presented in the results section, reveals a rapid and complex pattern of urban sprawl that raises questions about the sustainability of territorial development. Historically concentrated around its old city core and a productive agricultural belt, the city has gradually expanded toward the peripheries, leading to landscape fragmentation and a significant decline

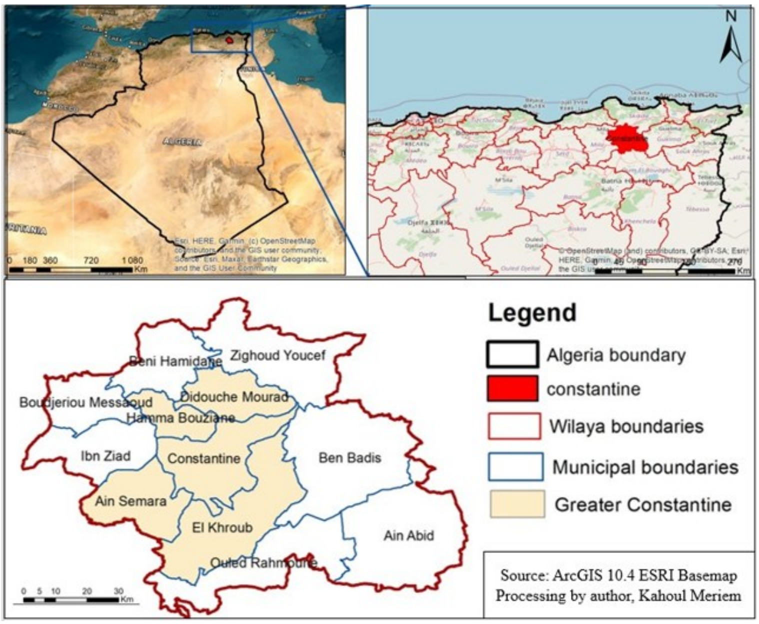

Figure 1. Geographical location of the studied area.

in vegetation cover. This dynamic reflects an increasing imbalance between the demand for housing and infrastructure and the preservation of natural areas, within a context of climate change that exacerbates pressures on local ecosystems.

UHIs areas where surface and air temperatures are significantly higher than surrounding rural zones have been extensively documented in rapidly urbanizing regions worldwide [6][7]. In Mediterranean and semi-arid cities, the combination of warm background climate, high solar radiation, and accelerated land artificialization creates particularly intense thermal anomalies [8]-[11]. North African cities are increasingly affected by these dynamics, where expanding impervious surfaces replace vegetated and agricultural land, exacerbating the UHI effect and threatening thermal comfort and public health [12][13]. Remote sensing -based indicators and GEE, notably NDVI, NDBI and LST, have proven effective tools for quantifying the spatial relationships between land cover and surface temperature in urban environments [14][15]. The objective of this study is to examine the interactions between land-use change, vegetation dynamics Normalized Difference Vegetation Index NDVI, and land surface temperature (LST), in order to assess the impact of urbanization on the microclimate of Constantine. To achieve this, a spatio-temporal approach based on the use of Landsat satellite imagery (1995–2024) and geospatial processing (GIS and remote sensing) was employed. This method allows for correlating land-use changes with thermal variations and quantifying the effects of land artificialization on the urban ecological structure. Through a cross-analysis of geographic, environmental, and urban dimensions, the study seeks to identify actionable strategies for more sustainable and resilient urban planning.

The choice of Greater Constantine as the study area is justified by its morphological, socio-economic, and environmental specificities. Located within a contrasting landscape of plateaus and valleys, the city is highly vulnerable to climatic imbalances induced by urbanization. Its rapid development, the coexistence of declining agricultural zones and unplanned peripheral urbanization, make it a relevant case study for understanding the interactions between urban sprawl, land artificialization, and microclimatic changes. At the regional scale, this case also illustrates the common challenges faced by arid and semi-arid cities of the Maghreb, which must reconcile urban growth with environmental preservation. Despite a growing body of literature on UHI dynamics in North African cities, few studies have specifically examined the multi-decadal trajectories of land artificialization, vegetation decline, and surface warming in intermediate-sized Algerian cities such as

Constantine, using a consistent remote sensing framework spanning nearly 30 years. In particular, the combined influence of land cover transitions, topographic heterogeneity, and episodic climatic events (such as El Niño) on LST dynamics in semi-arid Maghrebian cities remains insufficiently characterized. This study therefore addresses the following research question: To what extent has land artificialization in Greater Constantine (1995–2024) driven changes in vegetation cover and land surface temperature, and what is the relative contribution of built-up expansion versus vegetation loss to the observed thermal patterns?

2. MATERIALS AND METHODS

2.1. Study Area

Constantine, the third largest city in Algeria and the main metropolis of the country's eastern region, occupies a strategic position in the northeast of Algeria. The city serves as a major crossroads of the country's principal East–West and North–South transportation corridors, reinforcing its structuring role in the national territorial organization. The territory of "Greater Constantine," which constitutes the focus of this study, corresponds to an urbanized area extending over a radius of approximately fifteen kilometers and composed of five municipalities: the central city of Constantine and four peripheral communes forming satellite towns (Figure 1). These include Hamma Bouziane, located about 7 km to the north of Constantine; Didouche Mourad, also to the north and crossed by the East–West Highway; Aïn Smara, situated to the southwest about twenty kilometers away along the strategic axis linking Constantine, Sétif, and Algiers; and finally, El Khroub, located to the southeast at roughly 20 km from Constantine. Together, these municipalities form the Constantine urban cluster an administrative and functional entity playing a central role in local territorial management and planning [16].

The Constantine region has a Mediterranean semi-arid climate with continental influence, characterized by strong seasonal contrasts that are important for LST interpretation. Mean annual

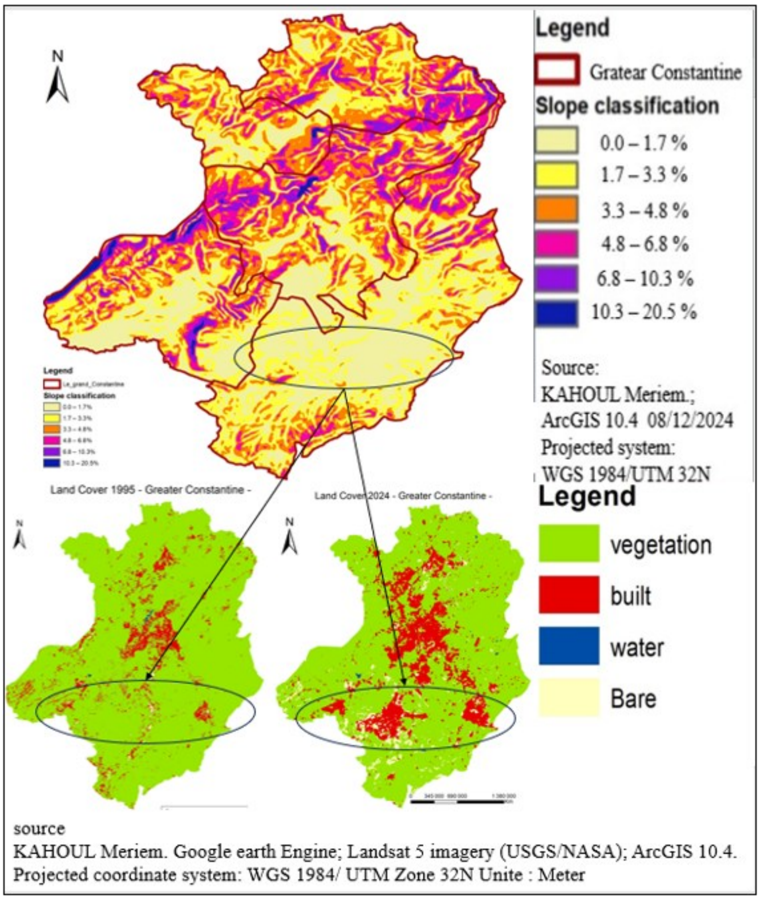

Figure 2. The topography of Greater Constantine.

Table 1. Details of satellite images and spectral bands used in this study.

Index / Parameter	Year(s)	Satellite / Sensor	Spatial Resolution	Bands Used (Wavelength Range)
LST	1995 / 2005	Landsat 5 TM	30 m (optical), 120 m (Band 6 thermal, resampled to 30 m)	B6 (Thermal Infrared): 10.40 – 12.50 µm
	2015 / 2024	Landsat 8 OLI/ TIRS and Landsat 9 OLI-2/TIRS -2	30 m (optical), 100 m (B10 thermal, resampled to 30 m)	ST_B10 (TIRS, Surface Temperature derived from Band 10): 10.60 – 11.19 µm
NDVI	1995 / 2005	Landsat 5 TM	30 m (optical), 120 m (Band 6 thermal, resampled to 30 m)	NIR (B4): 0.76 – 0.90 µm; Red (B3): 0.63 – 0.69 µm
	2015 / 2024	Landsat 8 OLI/ TIRS and Landsat 9 OLI-2/TIRS -2	30 m (optical), 100 m (Band 10 thermal, resampled to 30 m)	NIR (B5): 0.85 – 0.88 µm; Red (B4): 0.64 – 0.67 µm
Land Cover Classification	1995 / 2005	Landsat 5 TM	30 m (optical), 120 m (Band 6 thermal, resampled to 30 m)	B1 (Blue): 0.45 – 0.52 µm; B2 (Green): 0.52 – 0.60 µm; B3 (Red): 0.63 – 0.69 µm; B4 (NIR); B5 (SWIR1): 1.55 – 1.75 µm; B6 (TIR): 10.40 – 12.50 µm
	2015 / 2024	DYNAMIC WORLD dataset	—	—

temperatures range between 16.6 and 18.2 °C, with hot, dry summers (≈28 °C in July) and cooler winters (≈8–10 °C), indicating a high thermal amplitude [17]. Precipitation follows a wet (autumn–spring) and dry (summer) regime, typical of Mediterranean climates driven by winter disturbances and summer anticyclones [18]. These conditions favor strong surface heating and reduced evapotranspiration in summer, which amplifies urban heat island intensity and directly influences LST patterns [19].

Urban development in the study area is guided by regulatory instruments, notably the Master Plan for Development and Urban Planning (PDAU) and the Land Use Plan (POS), which define strategic orientations and land-use regulations. However, their implementation has coincided with rapid and sometimes poorly coordinated urban expansion, impacting urban morphology, environmental balance, and socio-economic structures. Urban growth has particularly affected agricultural lands in the southern part, forming new urban clusters independent of the main city core. This pattern reflects territorial polarization, facilitated by gentle slopes (0.0–1.7% to 1.7–3.3%) (Figure 2), which have eased construction and accelerated land conversion while partially containing informal settlements.

Over recent decades, urban expansion in Greater Constantine has induced significant ecological degradation, primarily through the loss of fertile and vegetated lands. From 1987 to 2020, approximately 3,000 ha—nearly 7% of the cultivable area were converted into built-up zones [20]. This process intensified after 2011, when regulatory reclassifications and expropriations led to the withdrawal of more than 2,600 ha for housing and public infrastructure. Subsequent major projects, such as the Constantine Ali Mendjeli tramway, the Béni Haroun dam, and the East–West Highway, further consumed agricultural land, bringing the total loss to around 3,678 ha. These transformations highlight the growing conflict between urban development needs and the preservation of environmental and agricultural resources [20]. This situation exacerbates ecological imbalances and intensifies phenomena related to the urban microclimate.

2.2. Data and Preprocessing

This study is based on temporal series from the Landsat satellite missions: Landsat 5 TM for the years 1995 and 2005, Landsat 8 OLI/TIRS (2015), and Landsat 9 OLI-2/TIRS-2 (2024) [21]. The satellite data were accessed through the Google Earth Engine (GEE) platform. These sensors provide a spatial resolution of 30 meters for optical bands and between 120 (Landsat 5) and 100 m (Landsat 8/9) for thermal bands. The latter were resampled to 30 m to ensure consistency with the spectral bands. The datasets used belong to Collection 2, Level 2 products (Surface Reflectance and Surface Temperature), which are radiometrically and geometrically corrected by the United States Geological Survey (USGS) [22].

2.3. Methodology

The methodological framework is structured around three main stages: the calculation of vegetation indices, the estimation of LST, and the supervised classification of land use and land cover (LULC). All processing steps were conducted within the GEE environment, using Landsat imagery provided by the USGS. Table 1 summarizes these stages and provides detailed information [23][24] on the satellite images and spectral bands used in this study. The use of two classification approaches reflects both data constraints and methodological progress. For 1995 and 2005, Landsat 5 TM imagery was classified using a supervised CART algorithm due to the absence of reliable pre-classified datasets. For 2015 and 2024, the study used the Dynamic World product derived from Sentinel-2 imagery, offering 10 m resolution and globally validated classifications based on deep learning [25]. However, this methodological difference introduces a potential comparability bias, which is considered when interpreting land cover changes.

For the years 1995 and 2005, the study utilized Landsat 5 datasets (Surface Reflectance: LANDSAT/LT05/C02/T1_L2; Top of Atmosphere: LANDSAT/LT05/C02/T1_TOA), while the 2015 and 2024 datasets were derived from Landsat 8/9 collections (LANDSAT/LC08/C02/T1_L2). The analysis period extended from February to May for NDVI computation and across the entire year for LST estimation. Selected scenes exhibited cloud cover below 20% for vegetation indices and below 10% for thermal series. As Landsat missions (5, 8, and 9) collect data exclusively during daylight hours, the thermal imagery used for land surface temperature (LST) retrieval reflects daytime conditions only.

The thermal bands of the Landsat sensors used in this study have native spatial resolutions lower than the 30 m optical bands: 120 m for Band 6 of Landsat 5 TM, and 100 m for Band 10 of Landsat 8/9 TIRS. Within the USGS Collection 2 Level-2 processing pipeline, these bands are resampled to 30 m using bilinear interpolation [26], ensuring geometric consistency across all spectral and thermal layers prior to any analysis in GEE. It should be noted that this resampling does not increase the intrinsic thermal resolving power of the original detectors; the effective spatial detail remains physically constrained by the native sensor footprint. Since all Collection 2 Level-2 products are delivered on a uniform 30 m grid, no further resampling was applied within GEE resampling [27][28].

2.3.1. Land Use / Land Cover Classification

Land use and land cover (LULC) classification for the years 1995 and 2005 was carried out using a supervised classification approach based on the

Table 2. Confusion Matrix of LULC Classification — Landsat 5 TM (1995).

Predicted \ Reference	Built-up	Vegetation	Cultivated	Bare Soil	Water	Total	UA (%)
Built-up	83	9	0	0	0	92	90.2
Vegetation	0	2511	0	4	0	2515	99.8
Cultivated	0	0	45	0	0	45	100.0
Bare Soil	0	35	0	218	0	253	86.2
Water	0	0	0	0	36	36	100.0
Total	83	2555	45	222	36	2941	
PA (%)	100.0	98.3	100.0	98.2	100.0		

Table 3. Confusion Matrix of LULC Classification — Landsat 5 TM (2005).

Predicted \ Reference	Built-up	Vegetation	Cultivated	Bare Soil	Water	Total	UA (%)
Built-up	**268**	**53**	**0**	**0**	**0**	**321**	**83.5**
Vegetation	1	705	3	0	0	709	99.4
Cultivated	0	2	19	0	0	21	90.5
Bare Soil	0	4	0	231	0	235	98.3
Water	0	2	0	2	26	30	86.7
Total	269	766	22	233	26	1316	
PA (%)	99.6	92.0	86.4	99.1	100.0		

Classification and Regression Tree (CART) algorithm implemented in GEE. Representative training samples for each land cover class were collected through visual photo-interpretation of Landsat 5 composite imagery, supported by ancillary topographic and cartographic data. A total of 470 training polygons were digitized across the five classes: vegetation (n = 189), bare soil (n = 128), cultivated land (n = 70), urban areas (n = 70), and water bodies (n = 13). All samples were collected at a scale of 30 m using the "sampleRegions()" function in GEE and merged into a single training dataset prior to classifier fitting. The CART classifier was implemented as "ee.Classifier.smileCart()" with a maximum of 10 nodes. Accuracy was assessed using a confusion matrix computed directly within GEE on withheld reference samples, yielding an Overall Accuracy and a Kappa coefficient. Five major classes were identified: urban areas, vegetation, cultivated land, bare soil, and water bodies. The resulting raster map was then converted into vector format to enable the quantification and spatial analysis of each class area within ArcGIS [29]. The land cover maps for 2015 and 2024 were generated from the Dynamic World dataset (GOOGLE/DYNAMICWORLD/V1) available on the GEE platform. This product, developed jointly by Google and the World Resources Institute (WRI), provides near real-time land cover classification at a 10-meter spatial resolution, derived from Sentinel-2 imagery. The resulting image was then clipped to the boundaries of the study area and exported as a GeoTIFF file for further spatial analysis [29]. The analysis primarily focused on vegetation (including natural areas and agricultural lands), urban zones, and bare soils to characterize urban and environmental dynamics.

2.3.2. Calculation of NDVI and LST Variables

The methodology adopted for analyzing vegetation and LST relied on a sequential remote sensing workflow using Landsat imagery acquired in 1995, 2005, 2015, and 2024. Landsat scenes were selected according to cloud cover conditions (<20%) and clipped to the study area boundaries. Surface reflectance products available in GEE were used for spectral index calculations. The Normalized Difference Vegetation Index (NDVI) was calculated for each image using Equation (1):

$$NDVI=\frac{NIR-RED}{NIR+RED} \quad \textbf{(1)}$$

where NIR and RED correspond to bands B4 and B3 for Landsat 5 TM, and B5 and B4 for Landsat 8/9 OLI-TIRS, respectively. Mean NDVI composites were generated and clipped to the study area.

The NDVI values were subsequently classified into vegetation-density classes to quantify the spatial distribution of vegetation cover. The area corresponding to each NDVI class was calculated using the pixelArea() function within GEE. Restricted to the study boundaries. From the NDVI, the fractional vegetation cover (Pv) was derived according to the Equation (2).

$$Pv=\left(\frac{NDVI-NDVImin}{NDVI\,max-NDVImin}\right)^2 \quad \textbf{(2)}$$

Normalized between 0 and 1, and subsequently used as a key parameter for emissivity correction, as shown in Equation (3).

$$\varepsilon = 0.004 \text{ x } P_V + 0.986 \quad \textbf{(3)}$$

Spectral emissivity (ε) was calculated from Pv

(Equation (3)) using the relationship proposed by Sobrino et al. [30], and brightness temperature was corrected to retrieve land surface temperature following the single-channel method of Jiménez-Muñoz and Sobrino [31].

Finally, LST was calculated using the single-channel algorithm, as shown in Equation (4);

$$LST = \frac{BT}{1 + \left(\frac{\lambda \times BT}{\rho}\right)\ln(\varepsilon)} \quad (4)$$

where, BT is brightness temperature (in Kelvin), λ is central wavelength of the thermal band (m), ρ is $h \cdot c/\sigma \approx 1.4388 \times 10^{-2}$ m·K (modified Planck's constant), and ε is land surface emissivity.

2.3.2.1. Landsat 5 TM (1995 & 2005)

The TOA Collection 2 product (LANDSAT/ LT05/C02/T1_TOA) was used, in which Band 6 (10.40–12.50 µm) is directly provided as at-satellite brightness temperature (BT, in Kelvin), computed by the USGS using thermal constants, as written in Equations (5) – (6) [32].

$$K1 = 607.76\ W \cdot m^{-2} \cdot sr^{-1} \cdot \mu m^{-1} \quad (5)$$

$$K1 = K2 = 1260.56\ K \quad (6)$$

BT was subsequently corrected for land surface emissivity using the Planck-based equation [13] to retrieve LST, converted to Celsius by subtracting 273.15.

2.3.2.2. Landsat 8/9 (2015 & 2024)

The Collection 2 Level-2 ST_B10 band (10.60–11.19 µm) was used directly, providing per-pixel emissivity-corrected surface temperature via the USGS Single-Channel algorithm. ST_B10 values were converted to Kelvin (scale factor: 0.00341802; offset: 149.0) then to Celsius. This methodology enables a precise and consistent estimation of vegetation dynamics and surface temperature variations within an urban context, providing a robust framework for environmental and urban studies. All of these steps were implemented as scripted workflows in Google Earth Engine to generate the NDVI and LST maps [31][33][34].

2.3.3. Statistical Analysis

Statistical analyses were conducted using GEE and Python to examine the relationships between LST, NDVI, and NDBI for each study year. NDBI was calculated directly in GEE using Landsat near-infrared and shortwave infrared bands. Approximately 5,000 pixels per year were extracted at 30 m resolution using random pixel sampling through the "ee.Image.sample()" function. The samples were exported and analyzed in Python using the scipy.stats library. Normality was assessed using the Kolmogorov–Smirnov test with Lilliefors correction, which indicated non-normal distributions for all variables ($p \leq 0.001$). Consequently, Spearman's rank correlation coefficient (ρ) was adopted as the primary statistical measure, while Pearson's correlation (r) was retained for comparison. Coefficients of determination (R^2) were calculated to quantify the proportion of LST variability explained by NDVI and NDBI. Given the large sample size ($n = 5{,}000$), statistical significance ($p < 0.001$) is expected for virtually any non-zero correlation; the coefficient of determination R^2 is therefore treated as the principal metric for assessing the practical strength of each relationship [35]. To limit the influence of spatial autocorrelation, a minimum spatial separation of approximately 90 m between neighboring pixels was considered during result interpretation.

3. RESULTS AND DISCUSSIONS

3.1. Land Cover Classification Accuracy Assessment

The accuracy assessment of the land cover classification for 1995 revealed an overall accuracy of 98.36% and a Kappa coefficient of 0.93. For 2005, the classification achieved an overall accuracy of 94.90% with a Kappa coefficient of

Table 4. Overall Accuracy and Kappa Coefficient of LULC Classification for 1995 and 2005.

Years	Overall Accuracy (%)	Kappa Coefficient
1995	98.37	0.93
2005	94.91	0.92

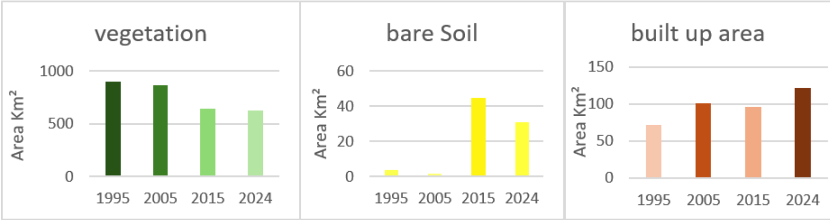

Figure 3. (a) vegetation changes in area between 1995and 2024. (b) Bare soil changes in area between 1995and 2024. (c) built up changes in area between 1995and 2024.

Table 5. Percentage changes in land cover classes between 1995 and 2024.

Class	Rate of change (%)
Vegetation	−30.05 %
Bare soils	+761.34 %
Built-up areas	+68.21 %

0.92, indicating a strong agreement between the classified map and the reference data (Table 2 - 4).

Regarding 2015 and 2024, the land cover maps were derived from the Dynamic World product (based on Sentinel-2 and available through GEE), a globally validated dataset widely used for large-scale land cover mapping and environmental monitoring. This ensures the reliability and comparability of the results across both time and space. The use of CART (Landsat 5, 30 m resolution) for 1995–2005 and Dynamic World (Sentinel-2, 10 m resolution) for 2015–2024 introduces a potential source of inter-temporal classification bias. The higher spatial resolution of Dynamic World may capture finer-scale land cover heterogeneity, potentially resulting in different class boundary delineations compared with the CART classification. In particular, the bare soil class — which showed the highest growth rate (+761%) — may be partially influenced by the differing spectral sensitivity and resolution of the two approaches. Bare mineral surfaces are spectrally similar to impervious urban areas in some Landsat TM bands, potentially causing commission errors in the CART classifier, whereas the higher-resolution Sentinel-2 data used in Dynamic World may discriminate these surfaces more accurately.

3.2. Temporal and Spatial Analysis of land Cover, NDVI and LST

3.2.1. Area Change Analysis

Figure 3(a) illustrates the distribution and temporal changes of vegetation in the Greater Constantine area for the years 1995, 2005, 2015, and 2024 while Figure 3(b) illustrates the distribution and temporal changes of Bare soil in the Greater Constantine area for the years 1995, 2005, 2015, and 2024. Figure 3(c) illustrates the distribution and temporal changes of built up in the Greater Constantine area for the years 1995, 2005, 2015, and 2024. Between 1995 and 2024, the Greater Constantine area underwent profound spatial transformations, reflecting a major shift inland-use dynamics. Table 5 shows the percentage changes in land cover classes between 1995 and 2024.

3.2.1.1. Vegetation Cover

Including both natural and agricultural areas, declined by about 30%, largely due to increasing urban pressure and the gradual conversion of farmland into residential and infrastructure zones. Despite this loss, certain agricultural areas were maintained, supported by local policies and the growing demand for food at the regional level. At the same time, bare soils experienced a sharp increase (+761%), expanding from 3.57 km² in 1995 to more than 30 km² in 2024. The substantial increase in bare-soil surfaces should be interpreted with caution, as it reflects both actual land-use transformations and methodological differences between the CART (1995–2005) and Dynamic World (2015–2024) classification approaches. Part of this increase is associated with vegetation degradation, soil erosion, construction activities, and demolition operations targeting precarious housing, which generated extensive transitional surfaces temporarily devoid of both vegetation and permanent built structures. In Constantine, the number of precarious settlements increased from 55 areas (6,266 dwellings) in 2008 to 65 areas (6,135 dwellings) in 2011, reflecting an intense phase of urban restructuring [36]. Another part of the observed increase may result from methodological differences between the CART classification applied to 30 m Landsat imagery and the finer-resolution Dynamic World product derived from 10 m Sentinel-2 data. The coarser Landsat resolution likely underestimated bare-soil surfaces in earlier periods due to mixed pixels, whereas Dynamic World more effectively captures transitional and interstitial bare areas. Consequently, the reported +761% increase should be considered an approximate upper-bound estimate rather than an exact measure of land-cover change.

3.2.1.2. Built-up Areas

Experienced a pronounced overall expansion of 68%, increasing from 72 km² in 1995 to 121 km² in 2024, largely reflecting sustained population growth and economic development This long-term urban expansion is supported by official housing statistics from the National Office of Statistics (ONS), which indicate that the total number of dwellings in Greater Constantine increased from 86,802 units in 1998 to 169,672 units in 2008, reaching 277,182 units in 2024 [1]. However, a temporary reduction in built-up surfaces is observed between 2005 (101 km²) and 2015 (96 km²), which represents a notable deviation from the general growth trend. This temporary decline represents a clear departure from the overall trend of continuous urban expansion. It can be primarily attributed to urban renewal and rehousing policies implemented during this period, which specifically targeted informal and precarious settlements. These interventions involved the demolition of low-density, spatially extensive individual housing, often characterized by irregular land occupation, and their replacement by more compact collective housing developments, particularly within planned urban extensions such as Ali Mendjeli [37]. In parallel, large-scale public investments were directed toward the construction of major transport infrastructure [38], public facilities, and serviced urban plots, which temporarily altered the spatial configuration of the built environment. While these policies initially led to a contraction of built-up surfaces between 2005 and 2015, they laid the groundwork for subsequent phases of intensified construction. After 2015, renewed housing programs, continued demographic pressure [39], and economic recovery stimulated a new cycle of urban growth, Algerian public policies, involving both public and private developers, have stimulated the supply of collective housing through programs such as AADL, established by Decree No. 91-148 of May 12, 1991, which experienced significant expansion after 2015 [40]. Resulting in accelerated land artificialization and a marked increase in built-up areas, which reached 121 km² by 2024. These changes illustrate a rapid urban dynamic that often occurred at the expense of ecological and agricultural balance, underlining the growing vulnerability of the Greater Constantine's ecosystems to anthropogenic pressures.

3.2.2. NDVI Analysis and Variations

The analysis of the NDVI maps obtained for 1995, 2005, 2015, and 2024 reveals a contrasting dynamic of vegetation cover. The NDVI values were divided into four classes [10]. NDVI < 0.2 : Non-vegetated areas (bare soils, artificial surfaces, or water bodies); 0.2 – 0.4 : Sparse and low-density vegetation; 0.4 – 0.6 : Moderate to semi-dense

Table 6. Temporal variation of NDVI statistics (maximum, minimum, and mean) in Greater Constantine, 1995–2024.

Year	1995	2005	2015	2024
max	0.868826568	0.848454535	0.88417286	0.87756997
min	-0.465088248	-0.49893239	-0.4869578	-0.39825523
mean	0.459092657	0.431062603	0.43323069	0.45704059

Table 7. Surface area of NDVI classes (1995–2024).

NDVI Classes	Area (km²)				Change 1995–2024 (km²)	Variation 1995–2024 (%)
	1995	2005	2015	2024		
-0,46 - 0	0,44	1,08	0,54	0,35	–0.09	–20.4 %
0 - 0,2	42,86	79 ,23	79,71	59,26	+16.39	+38.2 %
0,2 - 0,4	280,43	330,21	312,11	280,76	+0.33	+0.1 %
0,4 - 0,5	231,84	202,78	221,49	219,67	–12.17	–5.2 %
0,5 - 0,6	247,59	205,85	208,68	227,25	–20.34	–8.2 %
0,6 - 0,9	170,50	154,52	151,13	183,18	+12.67	+7.4 %

vegetation; NDVI ≥ 0.6 : Dense vegetation. Tables 6 and 7 present the statistical NDVI values (maximum, minimum, and mean) and the spatial distribution of vegetation by NDVI classes over the period 1995–2024; these datasets provide a comprehensive view of vegetation dynamics in the study area and its interactions with land artificialization. Table 6 provides a valuable overview of NDVI changes across the entire study area, allowing for quantification of overall vegetation dynamics. However, to assess the spatial distribution of NDVI and understand its territorial dynamics within the Greater Constantine region, an additional analysis was conducted. A corresponding table 07 was created showing the area of each NDVI class, which enables visualization of spatial patterns and supports the correlation of NDVI results with LST. This approach facilitates a comprehensive understanding of both the temporal and spatial dynamics of vegetation cover and its interaction with surface temperature.

The analysis of NDVI classes over the period 1995–2024, focusing on the February–May growing season, reveals contrasting dynamics across different vegetation types and non-vegetated areas. Non-vegetated surfaces (NDVI −0.46 to 0) remained largely stable, with only minor variations between periods, indicating the relative persistence of urban and bare mineral areas. Bare soils and sparsely vegetated areas (NDVI 0–0.2) showed a strong increase between 1995 and 2005, followed by stabilization and a slight decline between 2015 and 2024, reflecting urban expansion and partial land-use conversion. Areas corresponding to cereal crops and sparse vegetation (NDVI 0.2–0.4) increased until 2005, decreased slightly by 2015, and then stabilized, highlighting the resilience of agro-pastoral landscapes. Intermediate NDVI classes (0.4–0.6), representing dense crops and cereals in active growth, experienced notable declines between 1995 and 2005, followed by partial recovery, reflecting seasonal biomass variations and sensitivity to climatic and anthropogenic factors. Finally, dense vegetation and forested areas (NDVI 0.6–0.9) showed a slight decrease until 2015, before a marked increase in 2024, indicating localized reinforcement of forest stands and tree cover. This class plays a key role in regulating land surface temperature through shading and evapotranspiration. Overall, these results provide insight into the spatial distribution of vegetation, the temporal evolution of NDVI, and the potential relationships between NDVI and LST, emphasizing the crucial influence of vegetation type on surface temperature.

3.2.3. LST Variations

This section presents the spatiotemporal analysis of LST for the years 1995, 2005, 2015, and 2024, derived from thermal imagery processed within the GEE platform for the Greater Constantine region (Figure 4). In 1995, land surface temperatures varied between 13.36 °C and 27.35 °C, with a mean value of 21.39 °C, reflecting relatively moderate thermal conditions. By 2005, a clear warming trend had emerged, marked by an increase in minimum temperatures to 16.80 °C, a maximum of 32.35 °C, and an average of 25.60 °C. These values are consistent with MODIS Terra daily LST observations derived from Climate Engine, which reported a mean temperature of 25.31 °C for the same year, confirming the reliability of the Landsat-derived thermal patterns.

The year 2015 stands out as the period with the most pronounced thermal intensification across the study timeframe. During this year, surface temperatures reached a minimum of 23.20 °C, a maximum of 46.71 °C, and a mean of 35.51 °C. The physical plausibility of these extreme values is confirmed by independent MODIS Terra daily LST data (Climate Engine) in 2015, with a mean LST of 26.13 °C and maximum values 50.20 °C, supporting the physical plausibility of the Landsat-derived thermal anomaly despite differences in spatial resolution between Landsat and MODIS products. This substantial increase can be attributed to the combined effects of urban expansion and broader climatic drivers. The reduction of vegetated surfaces and the spread of impervious materials associated with rapid urbanization modify the surface energy balance by enhancing heat storage and limiting evapotranspiration, thereby reinforcing the urban heat island (UHI) effect. Similar patterns have been widely documented in North African cities, where impervious surfaces consistently exhibit the highest land surface temperature values. In addition, 2015 coincided with an exceptionally strong El Niño episode occurring within a context of ongoing global warming [41]. This climatic configuration generated widespread positive temperature anomalies at the continental scale, including in northern Algeria, intensifying extreme thermal conditions in the study area.

By 2024, a moderate decline in surface temperatures was observed, with minimum, maximum, and mean values decreasing to 22.16 °C, 43.94 °C, and 32.57 °C, respectively. and MODIS Terra data reported a mean temperature of 24.67 °C and maximum values close to 44 °C. Despite this attenuation, temperature levels remain markedly higher than those recorded in 1995 and 2005. To ensure consistency and facilitate comparison, a uniform temperature scale was applied to the map legends for all analyzed years (map5), allowing a coherent interpretation of spatial and temporal LST variations. Table 8 presents the percentage of spatial coverage of LST classes for each study year.

In maps a noticeable difference can be observed between 2015 and 2024, although the mean temperatures of the two periods are relatively close (35.5 °C in 2015 and 32.5 °C in 2024). This difference is mainly explained by the dominant temperature classes in each period. In 2015, the dominant temperature class was 34–37 °C, accounting for 46.1% of the spatial coverage and represented by the orange color on the map, followed by the 37–40 °C class, which covered 26.13% of the area and is shown in light red. In contrast, in 2024, the 37–40 °C class occupied only 1.53% of the spatial coverage, while the dominant class was 31–34 °C, representing 47.86% of the study area.

3.3. Analysis of the Relationship Between Land Cover, NDVI, and Land Surface Temperature (LST) Through Thematic Maps

To examine the relationship between urbanization, vegetation cover, and LST, a combined interpretation of the land cover, NDVI, and LST thematic maps was conducted. This integrated analysis allows for a spatial understanding of how land cover changes influence vegetation dynamics and surface thermal patterns over time. The thematic land-cover maps (Figure 5) indicate a substantial expansion of artificial surfaces between 1995 and 2024, with the most intense

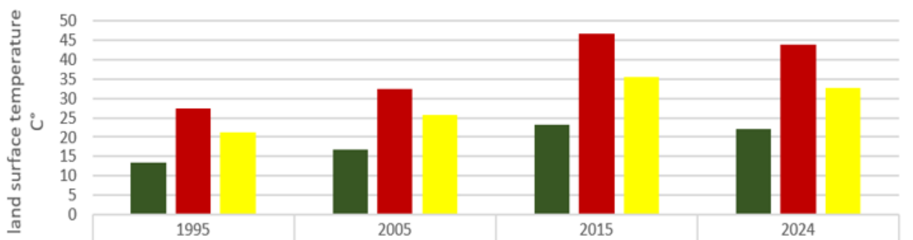

	1995	2005	2015	2024
T. min	13,361	16,8	23,2	22,16
T. max	27,35	32,35	46,71	43,94
T. mean	21,39	25,6	35,51	32,57

Figure 4. Land surface temperature dynamics (1995–2024).

Table 8. Percentage of the spatial coverage of land surface temperature (LST) classes.

Temperatures	1995	2005	2015	2024
13–16	0.54%	0%	0%	0%
16–19	10.76%	0.18%	0%	0%
19–22	47.04%	4.65%	0%	0%
22–25	40.6%	31.83%	0.011%	0.069%
25–28	1.06%	52.19%	0.092%	3.283%
28–31	0%	11.11%	3.128%	20.566%
31–34	0%	0.04%	22.689%	47.857%
34–37	0%	0%	46.095%	26.677%
37–40	0%	0%	26.129%	1.528%
40–43	0%	0%	1.827%	0.019%
43–46	0%	0%	0.0271%	0.001%
46–49	0%	0%	0.001%	0%
49–52	0%	0%	0.0009%	0%

transformation occurring during the 2005–2015 period. Urban growth was particularly concentrated in the southern and southwestern sectors, and to a lesser extent in the northwest, reflecting the development of major urban extensions. After 2015, the rate of artificialization appears to moderate, suggesting a relative stabilization of spatial expansion.

These changes are clearly reflected in the NDVI maps (Figure 6). Areas characterized by low NDVI values (0.0–0.2) expanded significantly in zones undergoing intense urbanization , particularly in the southwestern sector. Conversely, higher NDVI values (0.4–0.9), corresponding to vegetated and forested areas, remain concentrated mainly in the northeastern and southeastern parts of the study area. Spatial comparison of NDVI and LST maps reveals a differentiated thermal pattern. Built-up areas, represented in red on the land cover and NDVI maps, are characterized by low NDVI values (0–0.2) and moderate to high land surface temperatures ranging between 19-25C° in 1995 and 2005 and 28–37 °C in 2015 and 2024, confirming the significant role of impervious surfaces and land artificialization in increasing surface temperatures. In the northeastern and southeastern sectors particularly in the forested massifs of Djebel El Ouehch and Chaâttaba high NDVI values (0.5–0.9) correspond to surface temperatures below the annual mean ranging between 13–19 °C in 1995 and 2005, and between 25–28 °C in 2015 and 2024 (Figure 7), confirming the cooling role of dense and continuous vegetation. In contrast, several northern, northwestern, and southern zones exhibit relatively high NDVI values while maintaining elevated LST. This apparent inconsistency highlights the structural limitations of NDVI as a sole proxy for thermal regulation. In these areas, vegetation is predominantly seasonal and agricultural (mainly cereal crops), characterized by low canopy height and reduced evapotranspiration capacity. Such vegetation provides limited thermal buffering compared with dense, perennial tree cover, allowing surrounding artificial surfaces to dominate local thermal behavior.

The 2005–2015 period represents a critical phase in the observed thermal dynamics. A pronounced increase in bare-soil surfaces occurred during large-scale urban restructuring and demolition operations. Although the high percentage growth partly reflects a small baseline effect, it corresponds to a genuine spatial process linked to transitional land-cover states. These exposed mineral surfaces, characterized by low NDVI and high heat absorption capacity, contributed significantly to thermal amplification. This phase coincided with the strongest temperature increase recorded in the study (+9.91 °C), further intensified by exceptional climatic conditions, including the strong 2015 El Niño event. Beyond land cover, topographic and

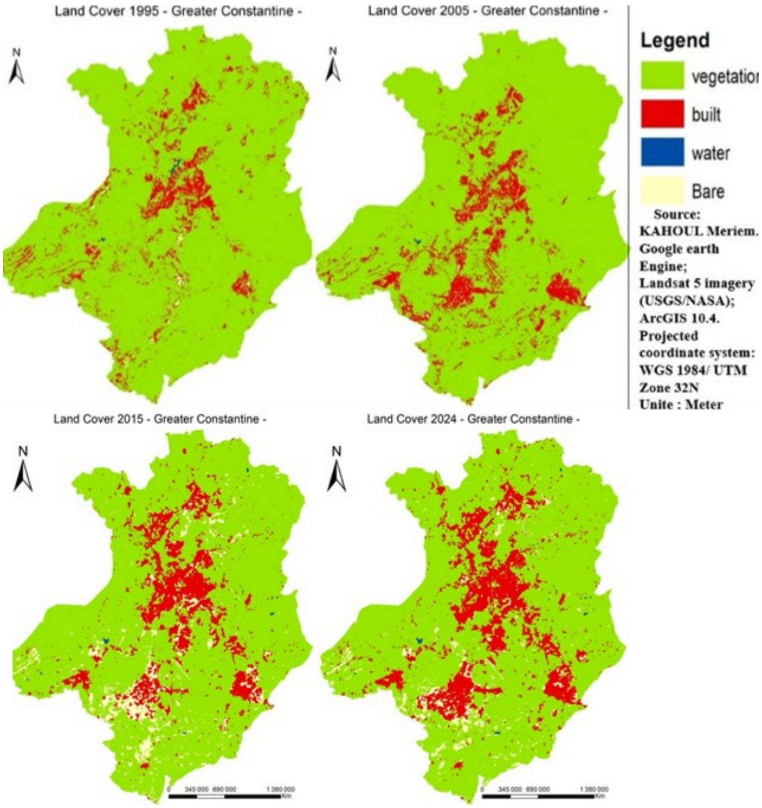

Figure 5. Land cover map 1995 – 2024.

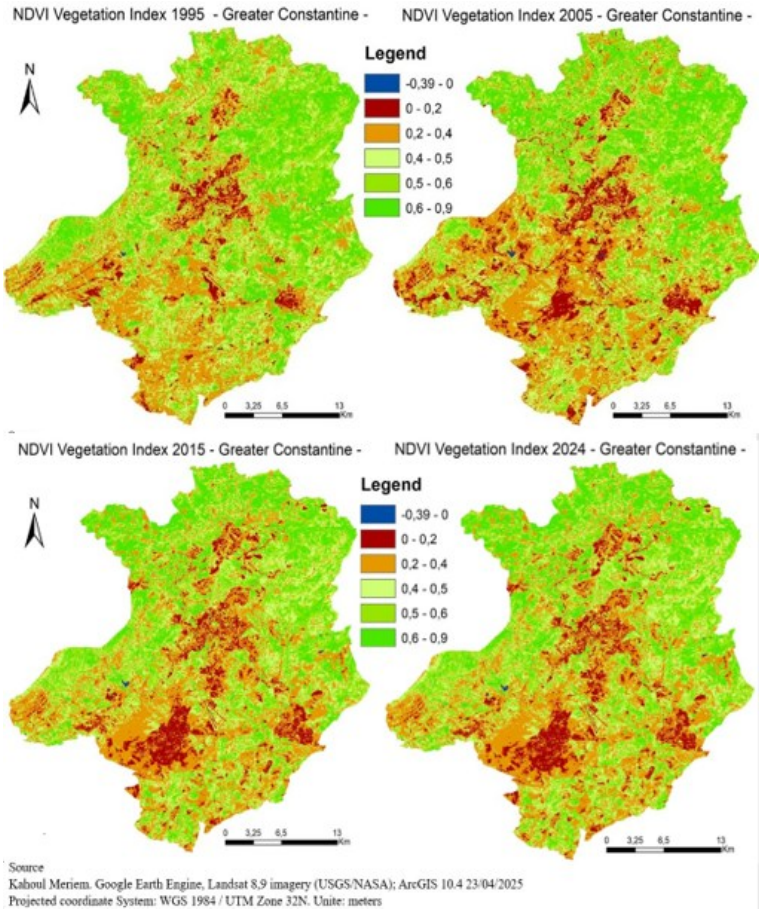

Figure 6. NDVI Values maps 1995 – 2024.

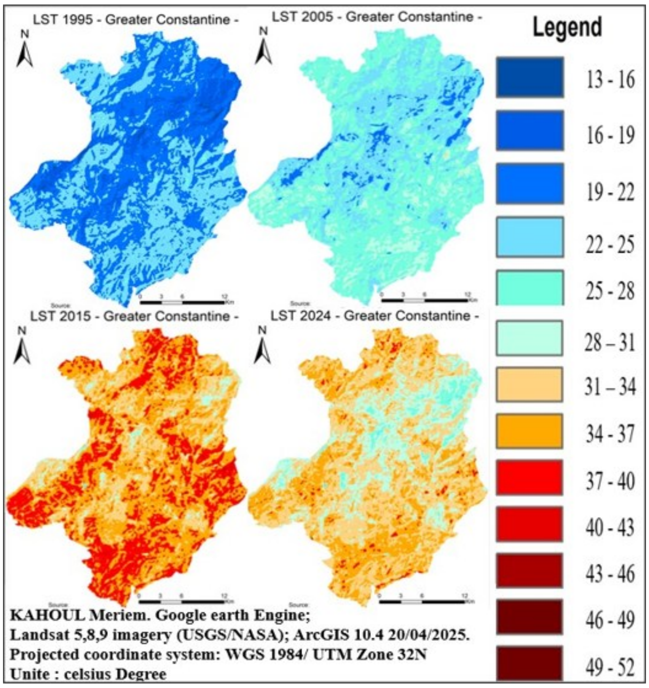

Figure 7. Land surface temperature LST map 1995-2024.

climatic factors further modulate spatial temperature distribution. Variations in elevation, slope, and aspect influence solar exposure and air circulation, generating localized thermal contrasts. Episodic climatic phenomena, such as heatwaves associated with El Niño and hot, dry sirocco winds originating from the Sahara, can temporarily intensify surface temperatures independently of local land-cover characteristics. These combined influences demonstrate that urban thermal patterns result from the interaction between artificialization, vegetation structure, transitional land surfaces, topography, and climatic variability.

3.4. Analysis of LST, NDVI, and NDBI Relationships Through Statistical Tests

3.4.1. LST– NDVI Correlation Analysis: Normality Assessment and Correlation Results

Normality assessment. Prior to computing correlation coefficients, the normality of NDVI and LST distributions was assessed for each study year using the Kolmogorov–Smirnov test with Lilliefors correction, applied to stratified random samples of $n = 5{,}000$ pixels per year. Results are presented in Table 9. The test rejected normality for both NDVI and LST across all study years ($p \leq 0.001$), consistent with the bimodal structure of urban landscapes where impervious hot surfaces and cooler vegetated areas form thermally distinct populations. Non-normality was particularly pronounced for NDVI ($D = 0.145$–0.187), reflecting the strong spectral contrast between built-up surfaces ($NDVI < 0.2$) and vegetated areas ($NDVI > 0.4$), while LST exhibited a right-skewed pattern ($D = 0.021$–0.073). Consequently, Spearman's rank correlation coefficient (ρ) was adopted as the primary statistical measure, with Pearson's r retained for comparative purposes given its asymptotic robustness for large samples ($n = 5{,}000$). The close directional agreement between both coefficients across all years confirms the robustness of the reported relationships regardless of distributional assumptions.

Spearman ρ is the primary measure (Table 10). Pearson r reported for comparison. $p < 0.001$ for all coefficients. 1995. A weak negative correlation ($\rho = -0.319$; $R^2 = 0.102$) indicates that vegetation explains only 10% of LST variability, reflecting the moderate urbanization level and limited thermal polarization between land cover types. In 2005, the strongest correlation across the study period ($\rho = -0.463$; $R^2 = 0.215$) shows vegetation explaining 21% of LST variability, driven by the growing spatial contrast between expanding impervious surfaces and remaining vegetated cover. In 2015, despite the highest recorded thermal intensification, the correlation weakened ($\rho = -0.337$; $R^2 = 0.114$), as the exceptional El Niño event elevated temperatures uniformly across all land cover types, temporarily overriding the local vegetation–temperature relationship. In 2024, a stable weak-to-moderate correlation ($\rho = -0.323$; $R^2 = 0.104$), comparable to 1995 despite higher urbanization, suggests that beyond a critical urban density threshold, further built-up expansion no longer strengthens the NDVI–LST relationship. Overall, the correlation analysis confirms a statistically significant inverse relationship between NDVI and LST for all study years ($\rho = -0.319$ to -0.463; $p < 0.001$) , indicating that areas with higher vegetation cover generally exhibit lower surface temperatures. However, the relatively low R^2 values 0.102–0.215 demonstrate that vegetation explains only 10–21% of LST spatial variability. This finding highlights that the NDVI–LST relationship is not exclusive nor sufficient to fully account for spatial temperature patterns. Other factors such as land cover composition, degree of surface artificialization, vegetation type, altitude, and regional climatic influences likely contribute substantially to the observed thermal behavior.

3.4.2. LST–NDBI Correlation Analysis: Normality Assessment and Correlation Results

Normality assessment: Prior to computing correlation coefficients, the normality of NDBI and LST distributions was assessed for each study year using the Kolmogorov–Smirnov test with Lilliefors correction, applied to stratified random samples of $n = 5{,}000$ pixels per year. Results are presented in Table 11. The test rejected normality for both NDBI and LST across all study years ($p \leq 0.001$), consistent with the bimodal structure of urban landscapes where high-density built-up surfaces (NDBI > 0) and vegetated or low-imperviousness areas (NDBI < 0) form two spectrally and thermally distinct populations incompatible with a Gaussian distribution. Non-normality was particularly pronounced for NDBI ($D = 0.118$–0.171), reflecting the strong spectral contrast between impervious surfaces and non-built-up land cover types, while LST exhibited a right-skewed pattern ($D = 0.040$–0.063) — a range slightly narrower than that observed for the NDVI–LST analysis, suggesting a marginally more homogeneous thermal distribution when stratified by built-up density. Consequently, Spearman's rank correlation coefficient (ρ) was adopted as the primary statistical measure, with Pearson's r retained for comparative purposes given its asymptotic robustness for large samples ($n = 5{,}000$).

The correlation analysis between LST and NDBI reveals a consistent positive relationship across all study years (Spearman $\rho = 0.519$–0.591; Pearson $r = 0.53$–0.60; $p < 0.001$), confirming that impervious surface expansion is a major driver of surface warming in Greater Constantine, through the high

Table 9. Results of the Kolmogorov–Smirnov Normality Test with Lilliefors Correction for NDVI and LST Variables Across the Study Years (1995-2024).

Year	Sample Size	NDVI D-stat	NDVI p-value	NDVI Normality	LST D-stat	LST p-value	LST Normality
1995	5000	0.186681	0.001	Not Normal	0.073168	0.001	Not Normal
2005	5000	0.144531	0.001	Not Normal	0.065530	0.001	Not Normal
2015	5000	0.147356	0.001	Not Normal	0.042049	0.001	Not Normal
2024	5000	0.146531	0.001	Not Normal	0.020746	0.001	Not Normal

D-stat = Lilliefors test statistic. H_0 (normality) rejected at $\alpha = 0.05$ for all years and both variables.

Table 10. LST–NDVI Correlation Results: Pearson r and Spearman ρ (1995–2024).

Year	Pearson r	Pearson R²	Spearman ρ	Spearman R²	p-value
1995	−0.360	0.130	−0.319	0.102	<0.001
2005	−0.566	0.320	−0.463	0.215	<0.001
2015	−0.461	0.213	−0.337	0.114	<0.001
2024	−0.438	0.192	−0.323	0.104	<0.001

Table 11. Results of the Kolmogorov–Smirnov Normality Test with Lilliefors Correction for NDBI and LST Variables Across the Study Years (1995-2024).

Year	Sample Size	NDVI D-stat	NDVI p-value	NDVI Normality	LST D-stat	LST p-value	LST Normality
1995	5000	0.171487	0.001	Not Normal	0.063154	0.001	Not Normal
2005	5000	0.117584	0.001	Not Normal	0.056926	0.001	Not Normal
2015	5000	0.126807	0.001	Not Normal	0.045222	0.001	Not Normal
2024	5000	0.129521	0.001	Not Normal	0.040150	0.001	Not Normal

D-stat = Lilliefors test statistic. H_0 (normality) rejected at $\alpha = 0.05$ for all years and both variables.

Table 12. LST–NDBI Correlation Results: Pearson r and Spearman ρ (1995–2024).

Year	Pearson r	Pearson R²	Spearman ρ	Spearman R²	p-value
1995	0.58	0.336	0.591	0.349	<0.001
2005	0.60	0.360	0.560	0.314	<0.001
2015	0.57	0.325	0.519	0.269	<0.001
2024	0.53	0.281	0.567	0.321	<0.001

heat storage capacity and negligible evapotranspiration of built-up materials (Table 12). With a sample size of $n = 5{,}000$ pixels per year, statistical significance ($p < 0.001$) is expected for virtually any non-zero correlation, regardless of its practical magnitude, due to the near-infinite statistical power of large samples. In this context, the p-value alone provides no meaningful information about the strength or practical importance of the NDBI–LST relationship. The coefficient of determination (R^2) — which quantifies the proportion of LST spatial variability explained by NDBI — is therefore the primary metric of interpretive interest [17]. Spearman R^2 values ranging from 0.269 to 0.349 indicate a moderate association, explaining between 27% and 35% of LST variability, while the remaining 65–73% is attributable to other spatial factors including urban morphology, surface albedo heterogeneity, topographic exposure, vegetation structure, and regional climatic forcing.

The strongest association was recorded in 1995 ($\rho = 0.591$; $R^2 = 0.349$), when sparse impervious surfaces generated marked thermal contrasts against the surrounding vegetated landscape. A slight decrease followed in 2005 ($\rho = 0.560$; $R^2 = 0.314$), and the lowest Spearman R^2 was observed in 2015 ($\rho = 0.519$; $R^2 = 0.269$), where the El Niño thermal anomaly broadly elevated temperatures across all land cover types, partially decoupling the NDBI–LST relationship. By 2024, Spearman ρ recovered to 0.567 ($R^2 = 0.321$), reflecting a more spatially consistent built-up–temperature relationship. Overall, surface artificialization is a stronger individual predictor of LST than vegetation loss ($R^2 = 0.269$–0.349 vs. 0.102–0.215; Section 3.4.1), though neither factor alone fully accounts for observed thermal variability, underscoring the need for multi-factor approaches in urban heat island analysis.

4. CONCLUSIONS

This study demonstrates that rapid urban expansion and increasing surface artificialization have been the primary drivers of land surface temperature (LST) intensification in Greater Constantine between 1995 and 2024. Using a standardized multi-temporal Landsat analysis implemented in Google Earth Engine, the results reveal substantial built-up expansion (+68.21%) and vegetation loss (−30.05%), accompanied by a marked increase in mean LST from 21.39 to 35.51 °C. Statistical analyses confirm that vegetation exerts a cooling effect, whereas impervious surfaces have a stronger and more consistent influence on thermal conditions, identifying urban artificialization as the dominant determinant of LST variability. Although the findings are subject to uncertainties related to Landsat spatial resolution and the use of different land-cover classification approaches across observation periods, the overall long-term trends remain robust. These results provide strong empirical evidence for integrating LST-based thermal risk assessments into urban planning, prioritizing green infrastructure expansion, urban canopy enhancement, and sustainable land management to mitigate urban heat in rapidly growing semi-arid Mediterranean cities.

AUTHOR INFORMATION

Corresponding Author

Kahoul Meriem — Laboratory for Quality of Use Assessment in Architecture and the Built Environment (LEQUArEB), Oum El Bouaghi University, Oum El Bouaghi-04000 (Algeria); Institute of Urban Techniques Management, Oum El Bouaghi University, Oum El Bouaghi-04000 (Algeria);

orcid.org/0009-0001-9149-3933

Email: meriem.kahoul@univ-oeb.dz

Authors

Mazouz Toufik — Laboratory for Quality of Use Assessment in Architecture and the Built Environment (LEQUArEB), Oum El Bouaghi University, Oum El Bouaghi-04000 (Algeria); Institute of Urban Techniques Management, Oum El Bouaghi University, Oum El Bouaghi-04000 (Algeria);

orcid.org/0000-0002-1591-3860

Kallab Debih Naouel — Institute of Urban Techniques Management, Oum El Bouaghi University, Oum El Bouaghi-04000 (Algeria);

orcid.org/0000-0001-6117-7545

Author Contributions

Conceptualization, Formal Analysis, Investigation, Resources, Data Curation, Project Administration, Funding Acquisition, Writing – Original Draft Preparation, Writing – Review & Editing, K. M.; Methodology, K. M., M. T., and K. D. N.; Validation, K. M. and M. T.; Visualization, Supervision, M. T. and K. D. N.

Conflicts of Interest

The authors declare no conflict of interest.

ACKNOWLEDGEMENT

The authors would like to express their deepest gratitude to the Evaluation of Use Quality in Architecture and the Built Environment Laboratory (LEQUAREB) University Larbi Ben Mhidi for funding this research.

DECLARATION OF GENERATIVE AI

During the preparation of this work, the author used AI Tools to assist in scientific writing and to revise certain paragraphs for clarity and academic style. After using this tool, the author reviewed, edited, and ensured the accuracy of the content, and takes full responsibility for the content of the publication.

REFERENCES

[1] F. A. Saidi, K. Phinzi, and E. Molnár. (2023). "Urbanization in Algeria: Toward a More Balanced and Sustainable Urban Network?". *Social Sciences.* **12** (3). 10.3390/socsci12030174.

[2] H. E. Remiki and F. Tahraoui. (2023). ""The Periphery – the Keystone of Rehousing in Algeria. The Case of Constantine City "". *Journal of Settlements and Spatial Planning.* **14** (1): 39-52. 10.24193/jssp.2023.1.04.

[3] H. Bourenane, Y. Bouhadad, and M. S. Guettouche. (2019). "Flood hazard mapping in urban area using the hydrogeomorphological approach: case study of the Boumerzoug and Rhumel alluvial plains (Constantine city, NE Algeria)". *Journal of African Earth Sciences.* **160**. 10.1016/j.jafrearsci.2019.103602.

[4] M. Khelili, N. Anoune, C. Haoues, A. Khedidja, N. Drifi, and K. Chorfi. (2025). "Multi-Criteria Evaluation of Land Suitability for Urban Extension Areas Identified in the PDAU of Setif City Using GIS and AHP". *International Journal of Geoinformatics.* 10.52939/ijg.v21i11.4603.

[5] R. Aoulmi and H. Boukerzaza. (2021). "Grand Constantine: A Multifunctional Peri-Urban Agriculture for Territorial Development". *Sciences Humaines.* 697-712.

PANDAWA INSTITUTE

[6] J. A. Voogt and T. R. Oke. (2003). "Thermal Remote Sensing of Urban Climates". *Remote Sensing of Environment.* **86** (3): 370-384. 10.1016/S0034-4257(03)00079-8.

[7] Q. Weng. (2009). "Thermal Infrared Remote Sensing for Urban Climate and Environmental Studies: Methods, Applications, and Trends". *ISPRS Journal of Photogrammetry and Remote Sensing.* **64** (4): 335-344. 10.1016/j.isprsjprs.2009.03.007.

[8] L. Zhao, X. Lee, R. B. Smith, and K. Oleson. (2014). "Strong Contributions of Local Background Climate to Urban Heat Islands". *Nature.* **511** (7508): 216-219. 10.1038/nature13462.

[9] M. Santamouris. (2020). "Recent Progress on Urban Overheating and Heat Island Research". *Energy and Buildings.* **207** 109482. 10.1016/j.enbuild.2019.109482.

[10] M. Morabito, A. Crisci, A. Messeri, S. Orlandini, A. Raschi, G. Maracchi, and M. Munafò. (2016). "The Impact of Built-Up Surfaces on Land Surface Temperatures in Italian Urban Areas". *Science of the Total Environment.* **551-552** : 317-326. 10.1016/j.scitotenv.2016.02.029.

[11] T. D. Mushore, J. Odindi, T. Dube, and O. Mutanga. (2017). "Prediction of Future Urban Surface Temperatures Using Medium Resolution Satellite Data in Harare Metropolitan City, Zimbabwe". *Building and Environment.* **122** : 397-410. 10.1016/j.buildenv.2017.06.033.

[12] L. Bounoua, J. Nigro, P. Zhang, K. Thome, and A. Lachir. (2018). "Mapping Urbanization in the United States from 2001 to 2011, with Natural Color Composites and the Normalized Difference Vegetation Index from the Moderate Resolution Imaging Spectroradiometer (MODIS)". *Remote Sensing.* **10** (9): 1500. 10.1016/j.apgeog.2017.12.002.

[13] A. Ameur, S. Ameur, and A. Adane. (2018). "Urban Heat Island Assessment and Investigation of Its Determinants Using Remote Sensing and GIS Tools in Algiers, Algeria". *International Journal of Remote Sensing.* **39** (4): 1055-1074. 10.1080/01431161.2017.1396145.

[14] S. Guha, H. Govil, A. Dey, and N. Gill. (2018). "Analytical Study of Land Surface Temperature with NDVI and NDBI Using Landsat 8 OLI and TIRS Data in Florence and Napoli, Italy". *European Journal of Remote Sensing.* **51** (1): 667-678. 10.1080/22797254.2018.1474494.

[15] Y. Zha, J. Gao, and S. Ni. (2003). "Use of Normalized Difference Built-Up Index in Automatically Mapping Urban Areas from TM Imagery". *International Journal of Remote Sensing.* **24** (3): 583-594. 10.1080/01431160304987.

[16] F. Bartolacci, R. Salvia, G. Quaranta, and L. Salvati. (2022). "Seeking the Optimal Dimension of Local Administrative Units: A Reflection on Urban Concentration and Changes in Municipal Size". *Sustainability.* **14** (22). 10.3390/su142215240.

[17] S. Sahabi Abed and A. Matzarakis. (2017). "Seasonal Regional Differentiation of Human Thermal Comfort Conditions in Algeria". *Advances in Meteorology.* **2017** : 1-14. 10.1155/2017/9193871.

[18] F. Giorgi and P. Lionello. (2008). "Climate Change Projections for the Mediterranean Region". *Global and Planetary Change.* **63** (2-3): 90-104. 10.1016/j.gloplacha.2007.09.005.

[19] C. Liu, S. Lu, J. Tian, L. Yin, L. Wang, and W. Zheng. (2024). "Research Overview on Urban Heat Islands Driven by Computational Intelligence". *Land.* **13** (12). 10.3390/land13122176.

[20] M. Allioua, "Les Abords de la Ville dans la Dynamique Urbaine : Cas de Constantine," Doctoral Dissertation, Université de Constantine, Constantine, Algeria, 2022.

[21] S. W. Myint, A. J. Brazel, and D. A. Quattrochi. (2013). "The Impact of Distinct Anthropogenic and Vegetation Features on Urban Warming". *Landscape Ecology.* **28** : 959-978. 10.1007/s10980-013-9868-y.

[22] S. Vahidi, V. Hatamzadeh, P. Nouri, and A. A. Far. (2023). "Monitoring Land Cover Changes in Tehran City (2018–2022) Using Remote Sensing-Based Spatial Information". *Asian Journal of Environment and Ecology.* **20** : 24-35. 10.9734/ajee/2023/v20i3440.

[23] C. Wang, M. Jia, N. Chen, and W. Wang. (2018). "Long-Term Surface Water Dynamics Analysis Based on Landsat Imagery and the Google Earth Engine Platform: A Case Study in the Middle Yangtze River Basin". *Remote Sensing.* **10** (10). 10.3390/rs10101635.

[24] Y. Zhou, J. Dong, X. Xiao, R. Liu, Z. Zou, G. Zhao, and Q. Ge. (2019). "Continuous monitoring of lake dynamics on the Mongolian Plateau using all available Landsat imagery and Google Earth Engine". *Science of the Total Environment.* **689** : 366-380. 10.1016/j.scitotenv.2019.06.341.

[25] C. F. Brown, S. P. Brumby, B. Guzder-Williams, T. Birch, S. B. Hyde, J. Mazzariello, W. Czerwinski, V. J. Pasquarella, R. Haertel, S. Ilyushchenko, K. Schwehr, M. Weisse, F. Stolle, C. Hanson, O. Guinan, R. Moore, and A. M. Tait. (2022). "Dynamic World, Near Real-Time Global 10 m Land Use Land Cover Mapping". *Scientific Data.* **9** (1): 251. 10.1038/s41597-022-01307-4.

[26] T. R. Loveland and J. R. Irons. (2016). "Landsat 8: The plans, the reality, and the legacy". *Remote Sensing of Environment.* **185** : 1-6. 10.1016/j.rse.2016.07.033.

[27] S. L. Ermida, P. Soares, V. Mantas, F. M. Göttsche, and I. F. Trigo. (2020). "Google Earth Engine Open-Source Code for Land Surface Temperature Estimation from the Landsat Series". *Remote Sensing.* **12** (9): 1471. 10.3390/rs12091471.

[28] J. Tavora, B. Jiang, T. Kiffney, G. Bourdin, P. C. Gray, L. S. Carvalho, G. Hesketh, K. M. Schild, L. F. Souza, D. C. Brady, and E. Boss. (2023). "Recipes for the Derivation of Water Quality Parameters Using the High-Spatial-Resolution Data from Sensors on Board Sentinel-2A, Sentinel-2B, Landsat-5, Landsat-7, Landsat-8, and Landsat-9 Satellites". *Journal of Remote Sensing.* **3**. 10.34133/remotesensing.0049.

[29] E. Giofandi, K. Munibah, K. Kraugusteeliana, A. Novalinda, and C. Sekarrini. (2023). "The Comparison of Vector and Raster Data for The Calculation of Landscape Environment Using a Geographic Information System Approach". *IT Journal Research and Development.* **7** (2): 209-219. 10.25299/itjrd.2023.10878.

[30] J. A. Sobrino, J. C. Jiménez-Muñoz, and L. Paolini. (2004). "Land Surface Temperature Retrieval from LANDSAT TM 5". *Remote Sensing of Environment.* **90** (4): 434-440. 10.1016/j.rse.2004.02.003.

[31] J. C. Jiménez-Muñoz and J. A. Sobrino. (2003). "A Generalized Single-Channel Method for Retrieving Land Surface Temperature from Remote Sensing Data". *Journal of Geophysical Research: Atmospheres.* **108** (D22): 4688. 10.1029/2003JD003480.

[32] C. J. Crawford, D. P. Roy, S. Arab, C. Barnes, E. Vermote, G. Hulley, A. Gerace, M. Choate, C. Engebretson, E. Micijevic, G. Schmidt, C. Anderson, M. Anderson, M. Bouchard, B. Cook, R. Dittmeier, D. Howard, C. Jenkerson, M. Kim, T. Kleyians, T. Maiersperger, C. Mueller, C. Neigh, L. Owen, B. Page, N. Pahlevan, R. Rengarajan, J.-C. Roger, K. Sayler, P. Scaramuzza, S. Skakun, L. Yan, H. K. Zhang, Z. Zhu, and S. Zahn. (2023). "The 50-year Landsat collection 2 archive". *Science of Remote Sensing.* **8**. 10.1016/j.srs.2023.100103.

[33] M. B. Moisa, B. T. Gabissa, L. B. Hinkosaa, I. N. Dejene, and D. O. Gemeda. (2022). "Analysis of Land Surface Temperature Using Geospatial Technologies in Gida Kiremu, Limu, and Amuru District, Western Ethiopia". *Artificial Intelligence in Agriculture.* **6** : 29-38. 10.1016/j.aiia.2022.06.002.

[34] C. D. Ursu. (2019). "The Land Surface Temperature Evolution (LST) Using Landsat Scenes: Case Study of the Industrial Platform Săvinești". *Geographia Technica.* **14** (2): 131-142. 10.21163/GT_2019.142.12.

[35] M. Lin, H. C. Lucas, and G. Shmueli. (2013). "Research Commentary—Too Big to Fail: Large Samples and the P-Value Problem". *Information Systems Research.* **24** (4): 906-917. 10.1287/isre.2013.0480.

[36] A. Benazzouz, R. Bouadam, and S. Belhanachi. (2023). "The Strategy for Eliminating Precarious Housing in Algeria to

Enhance Quality of Life: Case Study of Constantine". *YMER.* 1792-1811.

[37] S. Bensaada and T. Guerroudj. (2024). "Rehousing in Urban Renewal Projects in Constantine, Between Integration and Residential Satisfaction: Post-Occupancy Study of Rehousing Operations in Ali Mendjeli". *E3S Web of Conferences*. 10.1051/e3sconf/202458501014

[38] M. Boudjeriou and A. Kebiche. (2024). "The Arrival of the Tramway in Algeria: What Impacts on the City? Case Studies of the Oran and Constantine Tramways". *Papers of the Regional Science Association / Przegląd Geograficzny.* **69** (3). 10.48128/pisg-2024-69.3-03.

[39] A. Kadi and N. Mouhoubi. (2023). "Urbanization and Social Change in Algeria: Examining Demographic Shifts and Urban Growth Patterns". *İlköğretim Online.* **22** (3).

[40] R. Bensalem and A. Hadjiedj. (2024). "Housing Issue in Algeria: Can AADL Provide a Sustainable Solution?". *Revue Algérienne d'Économie et Management.*

[41] H. Herrera-Cervantes, G. Gutiérrez de Velasco, O. Zaytsev, E. D. Barton, and M. Gilcoto. (2023). "Anomalous thermal and winds condition drove low surface chlorophyll-a in La Paz Bay during the 2015–2016 El Niño event". *Estuarine, Coastal and Shelf Science.* **284**. 10.1016/j.ecss.2023.108280.